

Chapter 3

Correlation between fracture surface morphology and toughness in Zr-based bulk metallic glasses

Fracture surfaces of Zr-based bulk metallic glasses of various compositions tested in the as-cast and annealed conditions were analyzed using scanning electron microscopy. The tougher samples have shown highly jagged patterns at the beginning stage of crack propagation, and the length and roughness of this jagged pattern correlate well with the measured fracture toughness values. These jagged patterns, the main source of energy dissipation in the sample, are attributed to the formation of shear bands inside the sample. This observation provides strong evidence of significant “plastic zone” screening at the crack tip.

3.1 Introduction

Bulk Metallic Glasses (BMG's) fail without detectable plasticity when loaded in the absence of geometrical confinement, as, for example, in tension or in bending of plates with thicknesses greater than the material characteristic length scale [1,2]. For fracture toughness measurements, typical test geometries are compact tension (CT) and single edge notched bending (SENB). The loading geometry of both methods is bending of plates which are several millimeters thick. Considering that typical characteristic process zone sizes for BMG's are below 1 millimeter [3], one would expect BMG to exhibit poor toughness. However, fracture toughness data for Vitreloy 1 ($Zr_{41.2}Ti_{13.8}Cu_{12.5}Ni_{10}Be_{22.5}$) [4], the first commercial BMG alloy, taken from several reports suggest a range of fracture toughness that extends to values comparable to those of conventional crystalline metals, although the scatter associated with these data is significant. Specifically, the reported fracture toughness of Vitreloy 1 varies between 16 and 55 $MPa \cdot m^{1/2}$ [5-9]. In an additional study however in which single edge notched tension (SENT) was employed, the fracture toughness of Vitreloy 1 was reported to be in excess of 130 $MPa \cdot m^{1/2}$ [10]. Such an extremely high toughness is surprising, given that the tension loading geometry of SENT is geometrically less confined than the bending loading geometry of CT and SENB. The unusual combination of zero ductility but high fracture toughness of BMG's was also pointed out by Ashby and Greer [3]. The perceived high fracture toughness of metallic glasses has been attributed to the formation of a high density of shear bands at the crack tip [11]. However, this argument has only been supported by finite element analysis [12] and observation of shear band networks that evolved on the outer surfaces of specimens [5,10], although it is known that such surface shear bands only reflect the stress state of the free surface dominated by the plane stress condition.

In this study, the fracture surfaces of as-cast and annealed Zr-based BMGs of various compositions were carefully investigated to gain insight on how shear bands form in the regions of plane strain (far from the surface) and whether the extent of shear band propagation correlates to the measured fracture toughness. Various fracture samples from the Vitreloy alloy family were utilized in this study, including Vitreloy 1 ($\text{Zr}_{41.2}\text{Ti}_{13.8}\text{Cu}_{12.5}\text{Ni}_{10}\text{Be}_{22.5}$), Vitreloy 4 ($\text{Zr}_{46.75}\text{Ti}_{8.25}\text{Cu}_{7.5}\text{Ni}_{10}\text{Be}_{27.5}$), two different 4-component variants ($\text{Zr}_{33.5}\text{Ti}_{24}\text{Cu}_{15}\text{Be}_{27.5}$ and $\text{Zr}_{44}\text{Ti}_{11}\text{Cu}_{20}\text{Be}_{25}$) and a 6-component variant ($\text{Zr}_{44}\text{Ti}_{11}\text{Cu}_{9.3}\text{Ni}_{10.2}\text{Be}_{25}\text{Fe}_{0.5}$). Some of the $\text{Zr}_{44}\text{Ti}_{11}\text{Cu}_{20}\text{Be}_{25}$ samples were annealed at 3 different temperatures prior to testing. This wide variation in the chemical and thermodynamic state of the material produced a set of fracture toughness data (K_Q) that ranged from $6 \text{ MPa}\cdot\text{m}^{1/2}$ to $96.8 \text{ MPa}\cdot\text{m}^{1/2}$, enabling assessment of the key intrinsic material parameters that govern the fracture toughness of these materials. The effect of composition on fracture toughness was discussed in a separate report [13], while the effect of annealing will be discussed elsewhere. In the present study, fracture surface morphologies of specimens of varying composition and specimens with varying fracture toughness values will be investigated in an aim to explore the relationship between shear band propagation and toughness.

3.2 Experimental

Approximately 10g of arc melted BMG of the various compositions was cast into a Cu mold of nominal dimensions of $2.5 \text{ mm} \times 8 \text{ mm} \times 36 \text{ mm}$. The mold incorporated a 2 mm protrusion to form a notch. Lapping and polishing were performed to reduce the possible effect of residual stresses originating from the casting process, which resulted in specimen thicknesses of 1.9~2.2 mm. Fatigue pre-cracking and subsequent quasi-static loading for the determination of the critical load (P_Q) were performed using an MTS servohydraulic load frame equipped with a 3-

pt bend fixture with 31.75 mm span. The geometry of the SENB specimen and the definitions of several geometrical terms used in this study are shown in Figure 3-1(a). By applying a load corresponding to $\Delta K \cong 10 \text{ MPa}\cdot\text{m}^{1/2}$ and $K_{\min}/K_{\max} \cong 0.2$, a 1.1~2.4 mm long pre-crack was obtained after 40,000-150,000 cycles. Starting with an initial crack length of ~3.1-4.4 mm (the sum of the notch length and pre-crack), a quasi-static compressive displacement of 0.3 mm/min ($K \sim 40 \text{ MPa}\cdot\text{m}^{1/2}/\text{min}$) was applied and the load response of the pre-cracked sample was measured. Fracture toughness (K_Q) was calculated from the critical load using the formula given in ASTM E399.A3. It should be clarified that K_Q was used to denote fracture toughness rather than K_{IC} because the sample thickness did not guarantee plane strain condition in all cases (addressed later in this paper). The compositions and process conditions of the specimens used for this study, along with geometrical information such as specimen thickness and initial crack length (a_0), are listed in Table 3-1. Specimens are numbered in the order of decreasing K_Q in the first column of Table 3-1. These numbers will be used to refer to the specific specimens in this report.

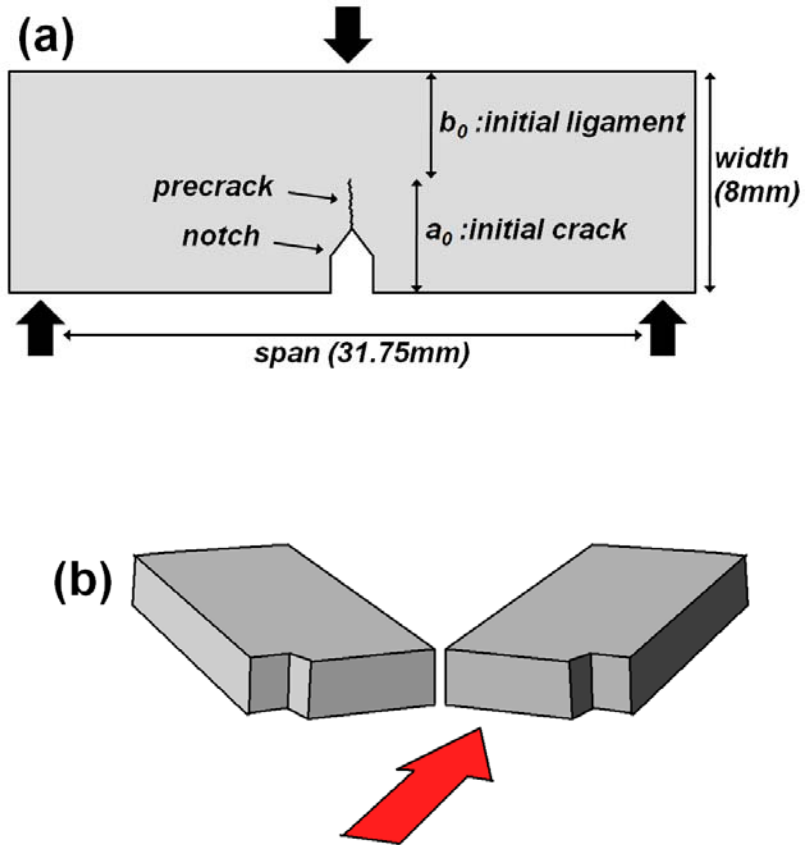


Figure 3-1. (a) Single edge notched bending fracture specimen geometry and dimension.

(b) Viewpoint of fracture surface observation after ultimate fracture.

Table 3-1. Experimental conditions and data of BMGs used in this study.

a_0 : initial crack length (a_0 = length of notch + length of fatigue pre-crack).

L_A : size of the plastic zone as defined in Figure 3-2(a).

The process zone size is calculated from $K_Q^2/\pi/\sigma_y^2$ (see Equation 3-2)

Sample No.	Composition	Annealing	thickness (mm)	Initial crack a_0 (mm)	K_Q (MPa·m ^{1/2})	L_A (mm)	σ_y (GPa)	Process zone size (μm)
S1	Zr _{33.5} Ti ₂₄ Cu ₁₅ Be _{27.5}	as cast	2.16	3.1	96.8	2.33	1.75	974
S2	Zr ₄₄ Ti ₁₁ Cu ₂₀ Be ₂₅	as cast	2.13	3.5	85.5	2.07	1.8	718
S3	Zr ₄₄ Ti ₁₁ Cu ₂₀ Be ₂₅	as cast	2.22	4.3	83.9	1.68	1.8	692
S4	Zr _{33.5} Ti ₂₄ Cu ₁₅ Be _{27.5}	as cast	2.19	4.4	80.8	1.69	1.75	679
S5	Zr _{41.2} Ti _{13.8} Ni ₁₀ Cu _{12.5} Be _{22.5}	as cast	2.18	3.8	74.4	1.95	1.86	509
S6	Zr _{33.5} Ti ₂₄ Cu ₁₅ Be _{27.5}	as cast	2.26	3.5	69.2	1.84	1.75	498
S7	Zr _{46.75} Ti _{8.25} Ni ₁₀ Cu _{7.5} Be _{27.5}	as cast	2.21	4.0	54.6	1.43	1.86	274
S8	Zr ₄₄ Ti ₁₁ Cu ₂₀ Be ₂₅	350°C 2hrs	2.12	3.9	51.3	1.58	-	259
S9	Zr _{41.2} Ti _{13.8} Ni ₁₀ Cu _{12.5} Be _{22.5}	as cast	1.86	3.2	49.6	1.59	1.86	226
S10	Zr ₄₄ Ti ₁₁ Ni _{10.2} Cu _{9.3} Be ₂₅ Fe _{0.5}	as cast	2.15	3.7	27.5	0	1.86	70
S11	Zr _{41.2} Ti _{13.8} Ni ₁₀ Cu _{12.5} Be _{22.5}	as cast	2.22	4.1	27.3	0	1.86	69
S12	Zr ₄₄ Ti ₁₁ Ni _{10.2} Cu _{9.3} Be ₂₅ Fe _{0.5}	as cast	2.16	3.7	26.4	0	1.86	64
S13	Zr ₄₄ Ti ₁₁ Cu ₂₀ Be ₂₅	320°C 25hrs	2.09	4.1	25	0	-	61
S14	Zr ₄₄ Ti ₁₁ Ni _{10.2} Cu _{9.3} Be ₂₅ Fe _{0.5}	as cast	2.16	3.4	21.7	0	1.86	43
S15	Zr ₄₄ Ti ₁₁ Cu ₂₀ Be ₂₅	290°C 62hrs	2.13	3.6	6	0	-	4

3.3 Fracture surface of bulk metallic glasses

Figure 3-2 shows the fracture surfaces of the various alloys studied. The viewpoint of observation is as described in Figure 3-1(b). The images in Figure 3-2 are arranged in the order of decreasing fracture toughness. The vertical arrows in all images point to the end of the pre-crack region. Beginning at the pre-crack, ultimate fracture occurred by crack propagation from right-to-left under monotonically increasing quasi-static load. The fracture surfaces of some specimens (Figure 3-2(a)-(e)) show highly jagged patterns at the beginning stage of crack propagation (region “A” in Figure 3-2(a)), and the length (“ L_A ” defined in Figure 3-2(a), listed in Table 3-1) and roughness of these jagged patterns are in good agreement with the measured fracture toughness values. This jagged region will be termed as ‘plastic zone’ hereafter. As fracture progresses these plastic zones (jagged patterns) disappear, and the rest of the fracture surface (region “B” in Figure 3-2(a)) shows the typical glassy metal dimple pattern, which is shown in Figure 3-3 and reported in many other studies [5-8,14-17]. The fracture surfaces of low fracture toughness specimens shown in Figure 3-2(f) and (g) don’t exhibit the characteristic rough topography in front of the pre-crack, and they appear to be uniformly filled with dimples created by mode I opening (Figure 3-3). The severe embrittlement caused by annealing the specimens for 2.5 days at 50°C below the glass transition temperature (T_g , 340°C measured by 20K/min DSC scan [13]) resulted in the fracture surface shown in Figure 3-2(h). This mirror-like fracture surface consists of hundred-nanometer sized dimples (Figure 3-3(d)), as observed by Xi et al. [14].

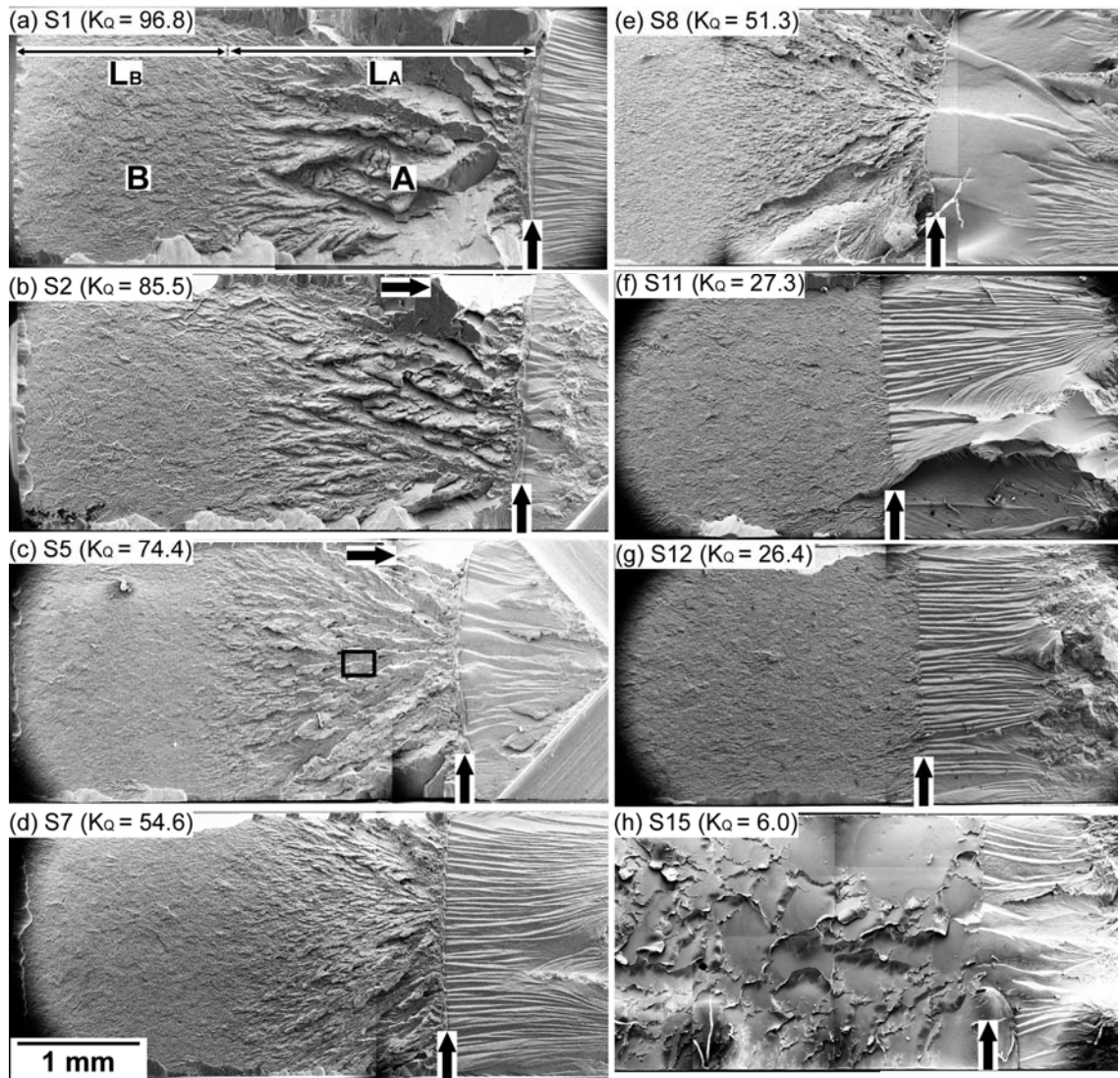
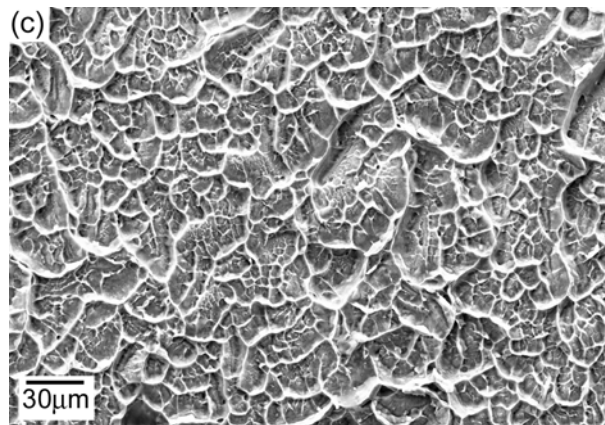
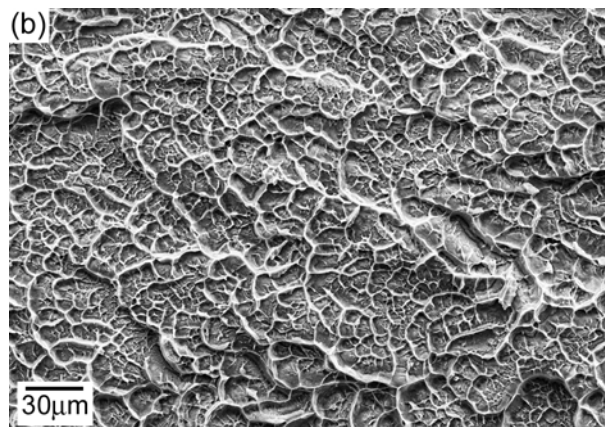
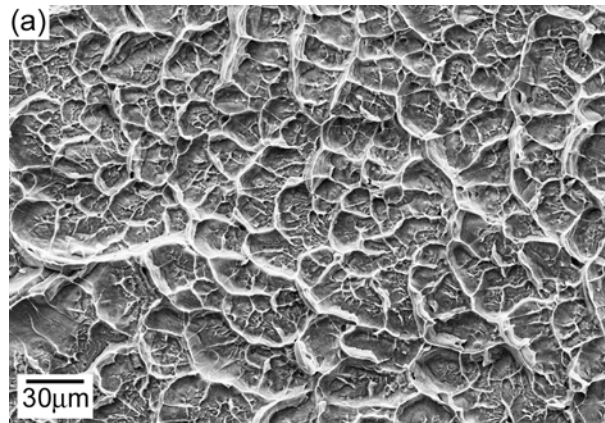


Figure 3-2. Scanning electron micrographs of the fracture surfaces. The vertical arrows mark the location of the initial pre-cracks. Crack propagation is from right to left in each micrograph. (a) specimen S1, (b) S2, (c) S5, (d) S7, (e) S8, (f) S11, (g) S12 and (h) S15. Measured fracture toughnesses (K_Q) are shown in the parentheses for all specimens.



(Figure 3-3. Continued)

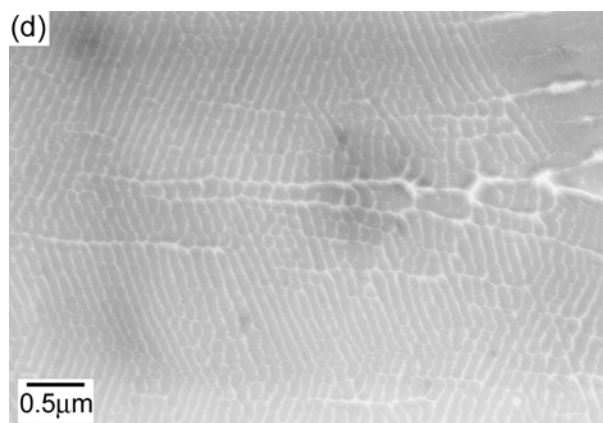


Figure 3-3. Fracture surface of area B (defined in Figure 3-2(a)). (a) specimen S2, (b) S7, (c) S10 and (d) S15.

3.4 Size of the dimple patterns

Dimple patterns of the BMG fracture surfaces (region “B” in Figure 3-2(a)) are shown in Figure 3-3. This region of the fracture surface is covered by isotropic dimples (no specific directionality) indicating that failure occurs by pure opening mode (Mode 1). Dimple patterns have been explained to form by massive flow of softened material at the crack tip [18] based on Taylor’s meniscus instability criterion applied to metallic glass fracture by Argon et al. [19] and the correlation between the process zone size and fracture energy recently proposed by Xi et al. [14]. It is noteworthy that even deeply embrittled BMG’s form dimple patterns, which is an indication that they undergo a certain degree of plastic flow prior to fracture (Figure 3-3(d)). The mean area of the dimples in Figure 3-3(d) is about $0.03\mu\text{m}^2$. However, the dimple size in Figures 3-3(a-c) is not unique, as small dimples reside inside large dimples, and the distinction between these two different dimple sizes is not clear. A distribution of dimple sizes suggests the occurrence of multiple coalescence events accompanied by a significant degree of cavity growth until the final fracture opening occurs. In other words, multiple cavitation events (nucleation of

cavities) and subsequent growth and coalescence of these cavities through plastic flow occur in front of a crack in a highly stressed BMG. Based on this observation, both the nucleation of cavities (which might be governed by the critical wavelength of the meniscus instability [19]) and the stability of the flow in the vicinity of nucleated cavity should be considered important contributing parameters to the fracture behavior. Despite the difficulty in quantifying the size distributions in these figures, it is obvious that the dimple sizes appearing in Figure 3-3(a) are larger than those in Figure 3-3(b) and (c), while the size difference between the dimples in Figure 3-3(b) and (c) is not significant. Likewise, the quaternary $Zr_{33.5}Ti_{24}Cu_{15}Be_{27.5}$ (S1, S4 and S6) and $Zr_{44}Ti_{11}Cu_{20}Be_{25}$ (S2 and S3) alloys listed in Table 3-1, which have K_Q ranging from 69.2 to $96.8MPa\cdot m^{1/2}$, consistently have patterns of larger dimple sizes comparable to the those shown in Figure 3-3(a), while the patterns of $Zr_{41.2}Ti_{13.8}Cu_{12.5}Ni_{10}Be_{22.5}$ (Vitreloy 1, S5, S9 and S11), $Zr_{46.75}Ti_{8.25}Cu_{7.5}Ni_{10}Be_{27.5}$ (Vitreloy 4, S7) and $Zr_{44}Ti_{11}Cu_{9.3}Ni_{10.2}Be_{25}Fe_{0.5}$ (S10, S12 and S14) alloys, which have K_Q ranging from 21.7 to $74.4MPa\cdot m^{1/2}$, are characterized by the smaller dimple sizes like those in Figure 3-3(b) and (c). Since the size of a dimple is a measure of BMG plastic flow prior to failure, a tendency of decreasing dimple size with decreasing fracture toughness is conceivable. Interestingly, BMG's that demonstrate a dimple size distribution similar to those in Figures 3-3(b) and (c), i.e. Vitreloy 1, Vitreloy 4 and $Zr_{44}Ti_{11}Cu_{9.3}Ni_{10.2}Be_{25}Fe_{0.5}$, exhibit fracture toughness that may be high or low depending on whether a plastic zone (the jagged zone in front of the pre-crack, defined by region "A" in Figure 3-2(a)) develops during fracture. Specifically, K_Q for these alloys ranges from 49.6 to $74.4MPa\cdot m^{1/2}$ if the fracture surface reveals a plastic zone, and from 21.7 to $27.5MPa\cdot m^{1/2}$ if no plastic zone develops. This behavior suggests that this class of BMGs can be either "tough" or "less tough", and this distinction is characterized by a tendency to develop a jagged plastic zone during fracture. Furthermore, it would be reasonable to assume that the mechanical energy spent

to generate this jagged plastic zone should be significantly more than the energy consumed to generate the dimples.

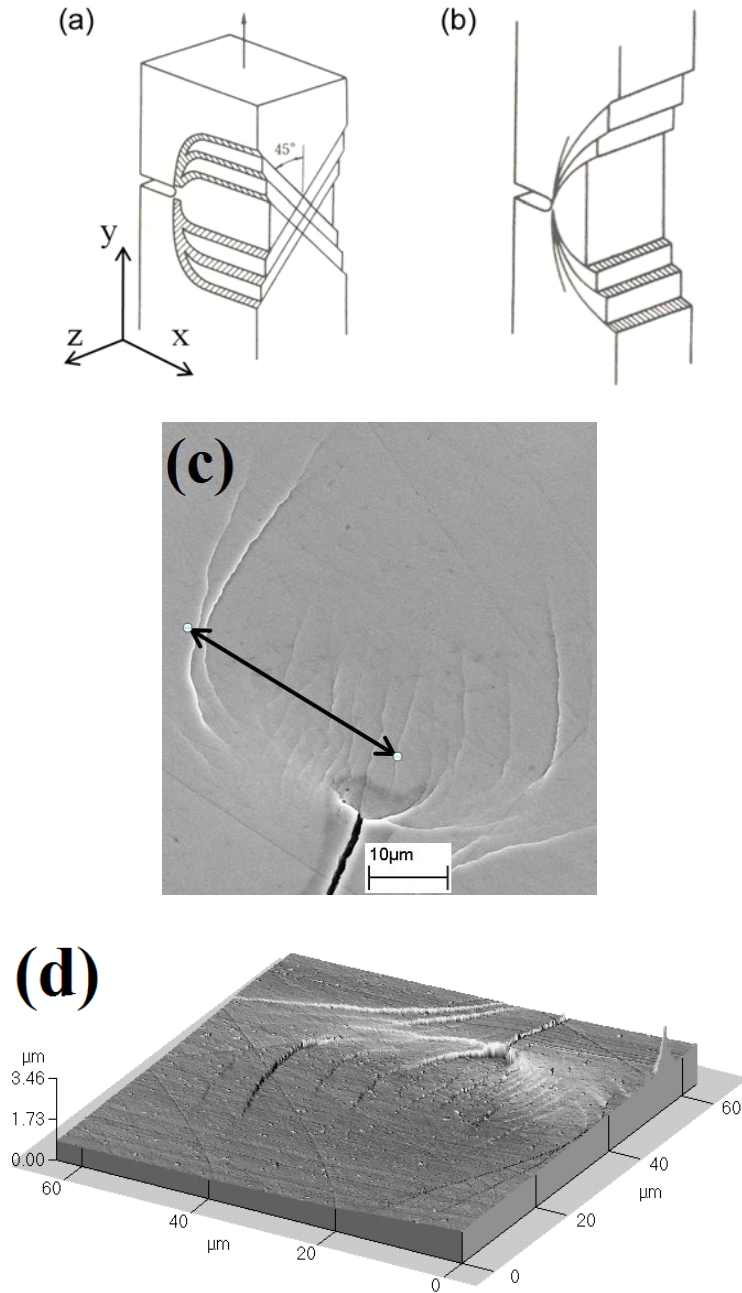


(Figure 3-4. Continued)

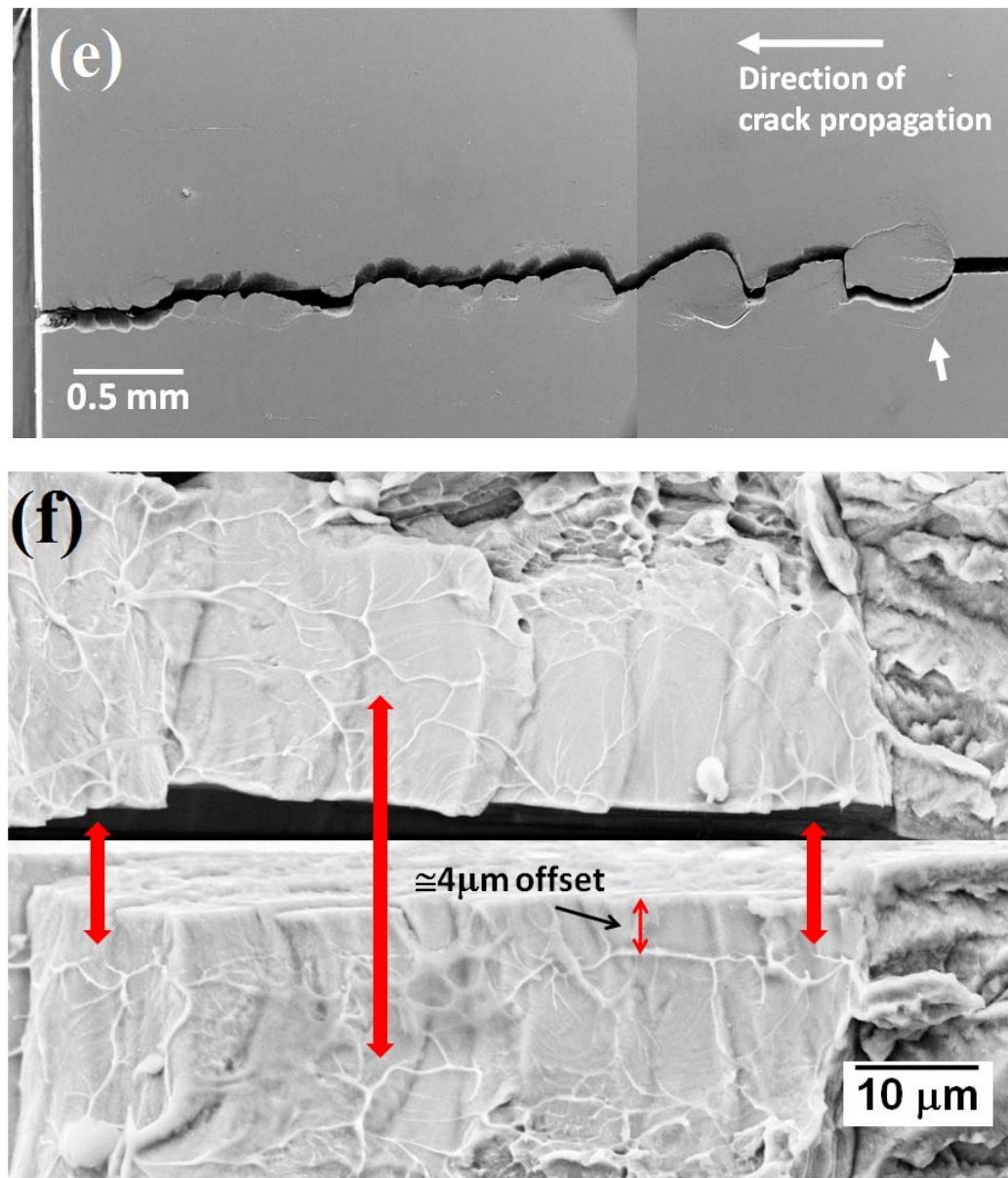
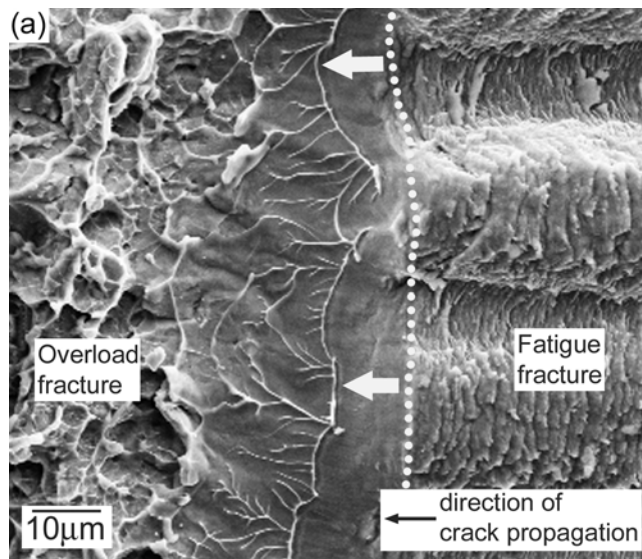


Figure 3-4. Direction of maximum shear stress and resultant slip in front of crack under mode I loading [20] under (a) plane stress condition and (b) plane strain condition. (c) Shape of a surface shear band formed around the crack tip (d) Atomic Force Microscopy (AFM) scan of the area shown in (c). (e) Wavy path of crack propagation on the surface of the specimen S2. (f) Fracture surface of specimen S9 on the area shown in (c) and (d).

3.5 Stress state around a crack tip (surface)

On the specimen surface, where the plane stress condition dominates, $\sigma_{zz}=0$. Since $\sigma_{yy} > \sigma_{xx} > \sigma_{zz}=0$, the maximum shear stress component is τ_{yz} as shown in Figure 3-4(a) [20]. The directions of x, y and z axes are defined in Figure 3-4(a). Figure 3-4(d) is a fast-scan AFM image of the area surrounding the pre-crack tip, shown in figure 3-4(c), opened under mode 1 loading. Figure 3-4(d) suggests that the shear offsets are directed into the thickness direction (z-direction), which is in agreement with the hypothesis of figure 3-4(a). The shear offsets appearing on the surface have also been observed to be directed into the thickness direction by Schneibel et al. [21]. Figure 3-4(e) shows the wavy path of a propagated crack on the surface of one of the tougher samples (specimen S2). At the beginning stage of ultimate fracture, the crack follows one of the shear bands distributed around the pre-crack tip, as indicated by the arrow in Figure 3-4(e). Figure 3-4(f) shows the matching surfaces of the fracture that occurred at this specific region (the arrow in Figure 3-4(e)) of specimen S9 (also, the area marked by horizontal arrows in Figure 3-2(b) and (c)). The fracture surfaces are filled with vein-like patterns, and these patterns look different from the typical dimple patterns shown in Figure 3-3. Vein-like patterns are generally observed from fracture surfaces generated by tensile loading conditions [22-25], under which single unstable shear band sliding occurs immediately before fracture. Unlike dimple patterns, which are characterized by isotropic, taller and thicker walls, vein patterns are characterized by shorter and thinner walls. Presumably, the difference in the two patterns can be attributed to a different BMG fluidity at the stage of ultimate fracture. The creation of a vein-like pattern would be associated with a higher fluidity originating from material softening during shear band sliding. Each arrow in Figure 3-4(f) connects the mating points at which the two opposite surfaces were attached before final fracture. From the lower surface in Figure 3-4(f), a shear band offset of about 4 μm can be observed. This observation also agrees well with Figure 3-4(a, c and d) in

terms of the direction of shear band propagation. It should be noted that the shear band pattern at the crack tip indicated by the arrow in Figure 3-4(e) and the fracture along one of these shear bands are only observed in the surface area shown by the horizontal arrows in Figure 3-2(b) and (c). Shear banding and fracture in interior of the specimen appears to be dominated by a different stress state.



(Figure 3-5. Continued)

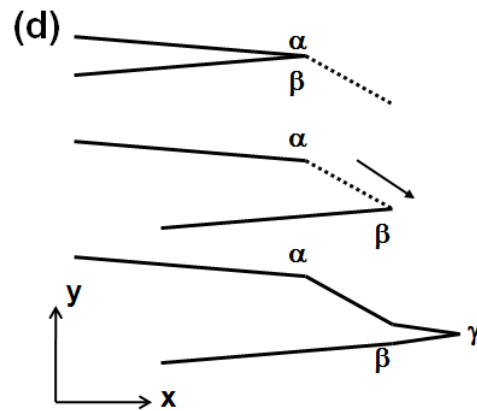
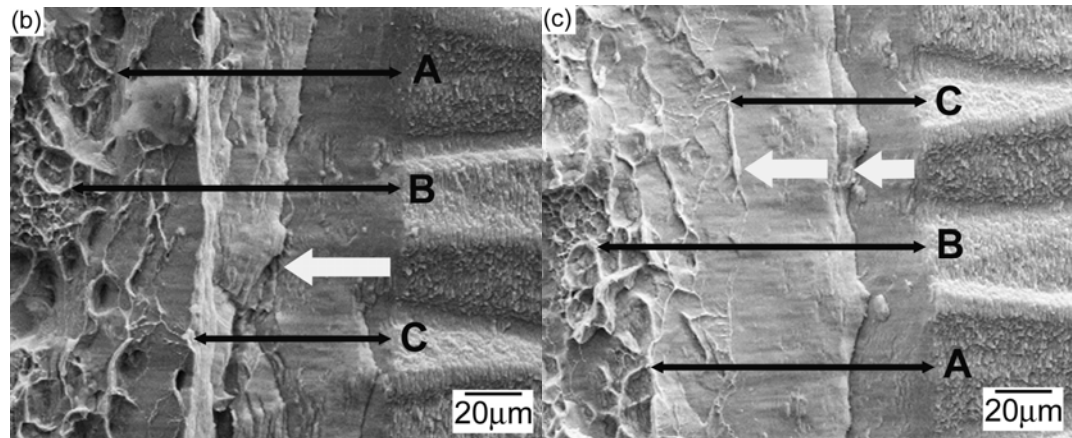


Figure 3-5. (a) boundary (dotted line) between fatigue pre-crack (right) and ultimate fracture (left) of specimen S5. Crack growth direction is from right to left. (b, c) matching surfaces of the boundary of specimen S1. (d) single shear band mechanism for blunting crack tip [17].

3.6 Stress state around a crack tip (interior)

The plane strain condition starts to dominate as the depth from the surface increases. In the plane strain condition, deformation along the z-direction (defined in Figure 3-4(a)) is confined such that the only shear direction available appears to be x-y direction as shown in Figure 3-4(b). A shear band pattern in front of crack tip, as shown in Figure 3-4(b), is also predicted by Tandaiya et al. [12]. Indeed, evidence of such shear band sliding is observed at the boundary between fatigue pre-crack and ultimate overload fracture. Figure 3-5(a) shows the boundary between fatigue pre-crack (right to the dotted line) and ultimate fracture (left to the dotted line) for specimen S5. The dotted line marks the pre-crack tip boundary before ultimate fracture. The crack growth direction is right to left. On the left of the pre-crack tip (dotted line), a smooth featureless region is observed (see thick arrow marks), followed by vein patterned region. This surface feature is pretty similar to the one shown in Figure 3-4(f), which suggests an evidence of shear band sliding and subsequent fracture. The direction of shear band sliding is indicated by the thick arrows. A possible shear banding mechanism for this fracture behavior was proposed by Tatschl et al. to explain crack tip blunting during loading [17] (see Figure 3-5(d)). This single shear band mechanism predicts that the distance between points α and γ and the distance between points β and γ (defined in Figure 3-5(d)) are different due to the shear band sliding. However, the matching surfaces of the specimen S1 shown in Figure 3-5(b) and (c) indicate that the distances of matching features (indicated by thin arrows A,B and C) from the pre-crack tip are almost the same despite the large amount of shear slip (more than $10\mu\text{m}$) marked by thick arrows. The single shear banding mechanism proposed in [17] (Figure 3-5(d)) therefore is not adequate to explain this behavior. One possible explanation is a combination of multiple shear bands. Flores and Dauskardt observed multiple steps ahead of the pre-crack [10, see their Figure 4(b)], which is also observed in this study.

The jagged surfaces (defined by the region “A” in Figure 3-2(a)) of the tougher samples shown in Figure 3-2(a)-(e) don’t appear to follow the deformation mode discussed above. The fracture surface shown in figure 3-2(a) has an inclination of about 45° with respect to the mode I loading direction, and agrees with Figure 3-4(a), not Figure 3-4(b). However, it should be noted that the specimen in Figure 3-2(a) may not be a perfect example, as it hardly show plane strain deformation occurring inside the sample due to the extensive surface shear banding that reaches almost to the center of the specimen. Other specimens, relatively less affected by the surface shear banding such as specimens in Figure 3-2(b)-(e), must provide better evidence for the plane strain behavior. Specimens in Figure 3-2(b)-(e) have rough and jagged surfaces as well, but the roughness doesn’t appear to result from shear band formation as clearly as Figure 3-2(a). However, careful observation reveals evidence of shear banding even on the less jagged surfaces of Figure 3-2(b)-(e). Figure 3-6 is a magnified image of the squared area marked in Figure 3-2(c). The fracture surface consists of steps running parallel to the crack propagation direction. As previously discussed, vein-like patterns on the surfaces (indicated by arrows) are observed on fracture surfaces generated by tensile loading [22-25]. Extensive shear band propagation (sliding) occurs up to a critical load at which the opening fracture process leads to ultimate fracture, generating the typical vein pattern. The rest of the fracture surface shown in Figure 3-6 resembles the typical dimple pattern of metallic glasses [5-8, 14-17], generated by direct opening without significant prior shear band sliding.

The evidence of shear banding inside the fracture specimen described above (and shown in Figure 3-6) is incongruent with the current understanding of crack tip plasticity [10, 12] in which the crack tip deformation behavior is described by Figure 3-4(b). The origin of the shear bands creating the jagged plastic zone is not clear yet, but this jagged zone has also been observed in other studies [6, 26-28]. “In some regions, these ridges were quite large and ran nominally

parallel to the direction of crack propagation [6, See their Figure 8(a) and 15].” Presumably, this shear band pattern shown in Figure 6 may be due to the morphology of the fatigue pre-crack. As shown in Figure 3-2, the fracture surface generated by fatigue pre-cracking has ridges running parallel to the crack growth direction. Magnified view of these fatigue fracture surface is given in Figure 3-5(a-c) to show that the surfaces have ‘ridge and furrow’ morphology directed normal to the crack front as well as the typical fatigue striations parallel to the crack front. This rough fatigue surface was also observed by Gilbert et al. [6, 17, 29]. Their surface, generated from $\Delta K \sim 10 \text{ MPa}\cdot\text{m}^{1/2}$ and $da/dN \sim 10^{-8} \text{ m/cycle}$, agrees with the fatigue pre-cracking condition used in this study. The roughness of the fatigue surfaces progressively diminishes with decreasing growth rates [29]. Even at slow growth rates, the ridges running parallel to the crack growth direction were reported [24, 30]. Irregularity due to kinks or steps along the crack front might cause a complex stress state in front of the crack and contribute to the jagged morphology. Indeed, Gao [31] performed an instability analysis of three-dimensional crack problem that included the shape perturbations parallel to the crack front to explain the ridge-like surface features running parallel to the crack growth direction as shown in Figure 3-5(a-c) and Figure 3-6. Gao studied the role of so-called T-stress term on determining crack front morphology. The stress intensity factor is the first term of the Irwin-Williams expansion of the crack tip stress field, and the second term is a constant stress contribution that acts over a longer distance from the crack tip, which is known as T-stress. The T-stress is known to affect the crack growth direction in two-dimensional crack propagation problem [32]. Hess and Dauskardt used Gao’s T-stress analysis to successfully model the surface morphology of fatigue fracture surface of BMG [30]. Additional study is required to understand the shear band pattern in the jagged plastic zone. It is important to note that the specimens without a plastic zone (Figure 3-2(f) and (g), specimens S10-S15) also have

nonplanar ridged fatigue fracture surfaces, which suggests that the nonplanar pre-crack front might be a necessary, but not a sufficient, condition for the formation of a jagged plastic zone.

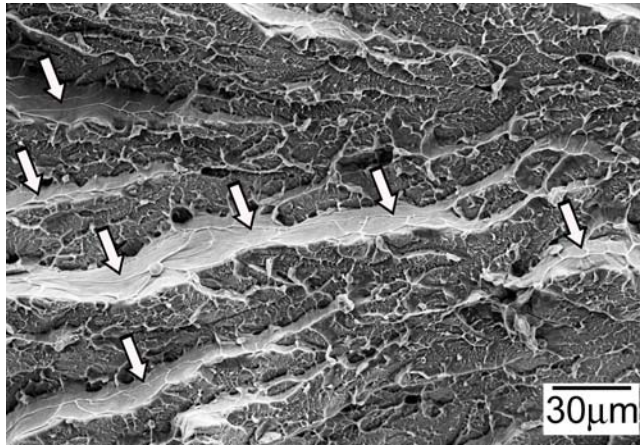


Figure 3-6. Magnified image of squared area in Figure 3-2(c).

3.7 Formation of the shear bands

A shear band that originates at the surface, where plane stress condition dominates, should be distinguished from one that originates inside the specimen, where plane strain condition prevails. This is because the formation of interior shear bands determines the validity of the measurement as plane strain fracture toughness (K_{IC}). Shear bands originating at the surface, which have the typical shape shown in Figure 3-4(c) and (d), propagate in the thickness direction. Figure 3-2(a) shows that these shear planes penetrate almost to the center of the specimen from both sides. It is also evident from Figure 3-2(b)-(c) that the plastic deformation originating at the surface propagates through a significant fraction of the specimen thickness (marked by horizontal arrows in Figure 3-2(b)-(c)). This suggests that the thickness of the specimens used in this study

is insufficient to satisfy the plane strain condition for the highly deformable and tough metallic glasses investigated here. However, the specimens in Figure 3-2(d) and (e) have a relatively small fraction of plane stress fracture surface. For the specimen S7 shown in Figure 3-2(d), the distance of the outermost shear band detectable by scanning electron microscopy (defined by the arrow in Figure 3-4(b)) was 130 μm , and the penetration depth of a surface shear band into the thickness direction (measured in Figure 3-2(d)) was about 160 μm . It is thus plausible that the bulk of the sample is far from the influence of surface shear bands, that is, the bulk of the sample could be under plane strain condition and the jagged pattern could be created by shear bands that originate within the sample, not at the surface.

BMG shear banding (i.e., localized plastic flow) occurs as a consequence of mechanical energy dissipation into the bulk glassy nanostructure, giving rise to local configurational changes that lead to a decrease in the local rigidity (i.e., local softening) [33] and eventual flow percolation along planes of maximum resolved shear stress. It is therefore reasonable to expect that shear bands will evolve within a bulk glassy nanostructure loaded in plain strain, and generation of these interior shear bands is argued here to be the origin of the jagged pattern formation observed in the images of Figure 3-2(b)-(e).

3.8 Effect of loading geometry

From the evidence gathered so far, the fracture process during a fracture test based on bending geometry such as CT and SENB is understood to progress by uniform spreading of a large number of shear bands, resulting in the development of a plastic zone within the test specimen (region “A” in Figure 3-2(a)), and ultimate fracture follows at the instant of critical load. It is reasonable to assume that the extension of the plastic zone (denoted as “ L_A ” in Figure 3-2(a))

is limited by the nature of the bending geometry of the CT and SENB test methods, as the remaining area (region “B” in Figure 3-2(a)) is loaded under compression during the test. Therefore, the fracture toughness value for Vitreloy 1, which is reported to be in excess of 130 MPa·m^{1/2} by the SENT method [10], may in fact be a reasonable estimate, because unlike the typical CT and SENB test geometry, the SENT test loading geometry is tension, which would drive the jagged region to cover the entire fracture surface, increasing the critical failure load dramatically resulting in a higher apparent fracture toughness.

3.9 Size of the plastic zone and the validity of K_Q as plane strain fracture toughness (K_{IC})

One of the ASTM size requirements for fracture toughness specimen is given by Equation 3-1, which implies that the size of the plastic zone must be less than 2% of the specimen dimensions in order to obtain a size-independent critical K_{IC} value [34].

$$B, a, (W-a) \geq 2.5 \cdot (K_Q/\sigma_y)^2 \quad \text{Equation 3-1.}$$

From Equation 3-1, the critical dimension for the specimen S7 with $K_Q=54.6\text{MPa}\cdot\text{m}^{1/2}$ and $\sigma_y=1.86\text{GPa}$ is 2.15mm, while the actual sample dimensions are $B=2.21\text{mm}$, $a=3.96\text{mm}$ and $b_0=4.04\text{mm}$ (initial ligament size, $b_0=W-a$). Thus, the measured K_Q value for this sample can be regarded as K_{IC} based on the specimen geometry. Other specimens listed below this sample in Table 3-1 (S8 to S15) satisfy the size requirement as well. It is worth noting however that the size of the plastic zone of specimen S7 measured from the image of Figure 3-2(d) (defined as “ L_A ” in Figure 3-2(a)) is 1.43mm, which is 35% of the initial ligament size b_0 . In Figure 3-7, the plastic zone region (L_A) acquired from the fracture surface of each sample is plotted against the process zone size, d , calculated from the measured K_Q and σ_y using Equation 3-2 below [3].

$$d = \frac{K_Q^2}{\pi \sigma_y^2} \quad \text{Equation 3-2.}$$

As seen from the plot in Figure 3-7, the length of the plastic zone region observed in the sample fracture surface correlates well with the plastic zone size estimated from the measured K_Q and σ_y , which suggests that the extent of the jagged pattern propagation is in essence a direct measure of the material fracture toughness.

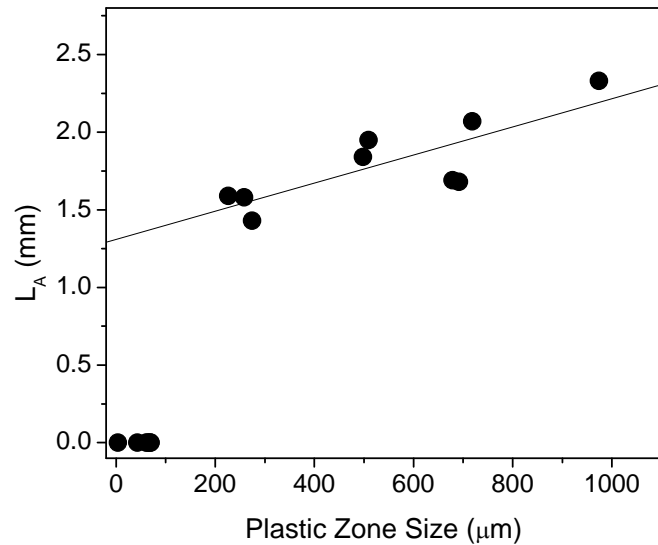


Figure 3-7. Correlation between jagged pattern extension (denoted as L_A in Figure 3-2(a)) and process zone size calculated from Equation 3-2 [3].

3.10 Possible effect of residual stress

Residual stress is known to affect fracture toughness significantly [35]. Residual stress develops during the casting process due to the high temperature gradients which arise during sample cooling and solidification. Compressive stress develops in the surface while tensile stress develops in the interior. The development of the plastic zone could be influenced by the residual stress. Generally, heat treatment below glass transition temperature is used to anneal out residual stress. In this study, the surfaces of all the as-cast test specimens were ground off in an attempt to remove the compressive region of the residual stress and produce a certain degree of relaxation. According to the viscoelastic model of Aydiner et al. [36], an 8.25mm thick Vitreloy 1 plate is estimated to develop up to -230MPa surface compression and +90MPa interior tension. However, an actual experiment by these authors revealed that a copper mold cast piece with the same thickness exhibited only -25 to -30MPa surface compression and +10 to +13 interior tension. In addition, the model suggested significant residual stress decreases with decreasing casting thickness. The casting thickness used in this study is 2.5mm. Their results also indicate that the compressive surface stresses are confined to a relatively thin surface layer. Therefore, removing ~10% of the surface layer is believed to reduce the residual stress to an insignificant level. Indeed, no difference in the size and shape of the plastic zone between as-cast (S7) and annealed (S8) specimens can be observed (See Figure 3-2(d) and (e)). Specimen S13 also exhibits exactly the same surface feature as those of other as-cast specimens (S10-12 and S14). Based on these comparisons, residual stress did not affect the results of this study.

3.11 Conclusions

In summary, in this study, the development of a significant “plastic zone” region during fracture of BMG samples that screens a crack tip was confirmed. The development of this jagged plastic zone region qualitatively and quantitatively explains why BMGs exhibit good toughness despite a near-zero ductility. Fracture surfaces were revealed showing that the roughness and the length of the jagged region adjacent to the pre-crack correlates well with the plastic zone size estimated from the measured fracture toughness values. The propagation of these jagged patterns, the main source of energy dissipation in the sample, was attributed to the ability of shear bands to form and propagate afar from the surfaces where plain strain conditions prevail. By recognizing that the jagged pattern is primarily the result of shear banding, it is understood that fracture toughness is closely related to the ability of the BMG to undergo a certain amount of plasticity prior to failing by catastrophic fracture.

Acknowledgements

The authors would like to thank Prof. G. Ravichandran of GALCIT, Caltech for providing the MTS test system. This work was supported in part by the MRSEC Program of the National Science Foundation under Award Number DMR-0520565.

References

- [1] Conner RD, Johnson WL, Paton NE, Nix WD. *J Appl Phys* 2003;94(2):904
- [2] Conner RD, Li Y, Nix WD, Johnson WD. *Acta Mater* 2004;52:2429
- [3] Ashby MF, Greer AL, *Scripta Mater* 2006;54:321

- [4] Peker A, Johnson WL. *Appl Phys Lett* 1993;63:2342
- [5] Lowhaphandu P, Lewandowski JJ. *Scripta Mater* 1998;38:1811.
- [6] Gilbert CJ, Schroeder V, Ritchie RO. *Met Mat Trans* 1999;30A:1739
- [7] Suh D, Dauskardt RH. *J Non-Cryst Solids* 2003;317:181
- [8] Suh D, Dauskardt RH. *Ann Chim Sci Mat* 2002;27:25
- [9] Conner RD, Rosakis AJ, Johnson WL, Owen DM. *Scripta Mater* 1997;37:1373
- [10] Flores KM, Dauskardt RH. *Scripta Mater* 1999;41:937
- [11] Johnson WL. *MRS Bulletin* 1999;24(10):42
- [12] Tandaiya P, Narasimhan R, Ramamurty U. *Acta Mater* 2007;55:6541
- [13] Kim CP, Suh JY, Wiest A, Lind ML, Conner RD, Johnson WL. *Scripta Mater* 2008;60:80
- [14] Xi XK, Zhao DQ, Pan MX, Wang WH, Wu Y, Lewandowski JJ. *Phys Rev Lett* 2005;94:125510
- [15] Lewandowski JJ, Wang WH, Greer AL. *Phil Mag Lett* 2005;85:77
- [16] Gilbert CJ, Ritchie RO, Johnson WL. *Appl Phys Lett* 1997;71:476
- [17] Tatschl A, Gilbert CJ, Schroeder V, Pippan R, Ritchie RO. *J Mater Res* 2000;15:898
- [18] Schuh CA, Hufnagel TC, Ramamurty U. *Acta Mater* 2007;55:4067
- [19] Argon AS, Salama M. *Mater Sci Eng* 1976;23:219
- [20] Hahn GT, Rosenfield AR. *Acta Metall* 1965;13:293
- [21] Schneibel JH, Horton JA, Munroe PR. *Metall Mater Trans* 2001;32A:2819
- [22] Spaepen F, Turnbull D. *Scripta Metall* 1974;8:563
- [23] Leamy HJ, Chen HS, Wang TT. *Metall Trans* 1972;3:699
- [24] Alpas AT, Edwards L, Reid CN. *Metall Trans A* 1989;20A:1395
- [25] Zhang ZF, Eckert J, Schultz L. *Acta Mater* 2003;51:1167
- [26] Davis LA. *Metall Trans A* 1979;10A:235

- [27] Lowhaphandu P, Ludrosky LA, Montgomery SL, Lewandowski JJ. *Intermetallics* 2000;8:487
- [28] Nagendra N, Ramamurty U, Goh TT, Li Y. *Acta Mater* 2000;48:2603
- [29] Gilbert CJ, Lippmann JM, Ritchie RO. *Scripta Mater* 1998;38:537
- [30] Hess PA, Dauskardt RH. *Acta Mater* 2004;52:3525
- [31] Gao H. *J Appl Mech* 1992;59:335
- [32] Cotterell B, Rice JR. *Int J Fract* 1980;16:155
- [33] Harmon JS, Demetriou MD, Johnson WL, Samwer K. *Phys Rev. Lett* 2007;99:135502
- [34] Anderson TL. *Fracture Mechanics: Fundamentals and Applications*, 1st ed.: CRC Press, 1991. p.431.
- [35] Launey ME, Busch R, Kruzic JJ. *Acta Mater* 2008;56:500
- [36] Aydiner CC, Ustundag E, Prime MB, Peker A. *J Non-Cryst Solids* 2003;316:82

Chapter 4

Effect of annealing on fracture toughness of a Zr-based Be-bearing bulk metallic glass

The $\text{Zr}_{44}\text{Ti}_{11}\text{Cu}_{20}\text{Be}_{25}$ alloy with as-cast fracture toughness $K_Q = 85 \text{ MPa}\cdot\text{m}^{1/2}$ is annealed at three different temperatures. Fracture toughness is found to decrease linearly as the annealing temperature decreases and the glass relaxes into lower energy configurations. When annealed at 290°C , 50°C below T_g , the fracture toughness drops to $6 \text{ MPa}\cdot\text{m}^{1/2}$, while the glassy structure is retained. This annealing embrittlement behavior is discussed together with the change of elastic properties.

4.1 Introduction

The structure of Bulk Metallic Glass (BMG) is bound to relax to some equilibrium liquid state, since the vitrification process called glass transition causes the liquid structure to deviate from its instantaneous equilibrium state at some temperature, termed the glass transition temperature, T_g . As shown in Figure 4-1 [1], the as-cast BMG structure is essentially a frozen liquid structure that has deviated from its equilibrium structure, depicted by dotted line, and is therefore bound to relax back to the equilibrium state via a thermally activated relaxation process.

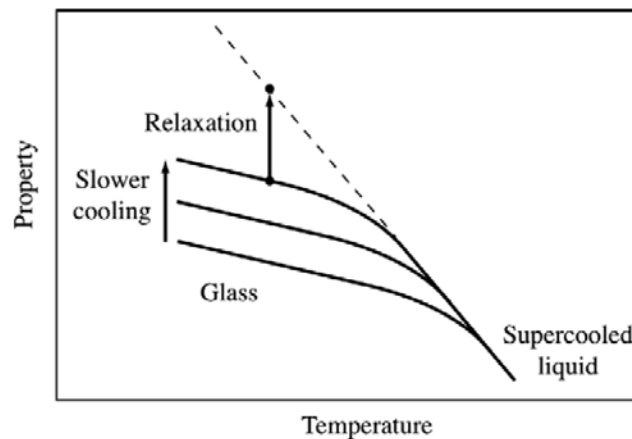


Figure 4-1. Schematic diagram of structural relaxation of BMG taken from Ref. 1. As temperature decreases, the supercooled liquid deviates from the equilibrium behavior at the glass transition point, and this deviation depends on the cooling rate.

This structural relaxation has been known to give rise to embrittlement of the BMG [2-6]. Suh and Dauskardt [2,3] and Launey et al. [6] used plane strain fracture toughness measurement (K_{IC}) to study the embrittlement behavior of Vitreloy 1 ($Zr_{41.2}Ti_{13.8}Cu_{12.5}Ni_{10}Be_{22.5}$) [7] and

Vitreloy 1b ($Zr_{44}Ti_{11}Ni_{10.2}Cu_{9.8}Be_{25}$) [8], respectively. The severe reduction of ductility and fracture toughness has been attributed to the reduction of free volume [2-6]. A reduction of free volume is known to hinder plastic deformation (shear banding) of the BMG, thereby reducing fracture toughness. This is a plausible argument, as suppressing the ability of the BMG to plastically deform leads to lower fracture toughness, as shown in Chapters 2 and 3.

In several recent rheological/ultrasonic studies, it has been demonstrated that a one-to-one correspondence exists between the configurational energy state of the BMG (determined by annealing temperature and time) and the isoconfigurational shear modulus [9-11]. More interestingly though, a functional relationship between viscosity and isoconfigurational shear modulus has been demonstrated in those studies [9-11], which implies a one-to-one correspondence between shear modulus and the activation barrier for configurational hopping, which determines the ability of the BMG to plastically flow.

In this study, the change in fracture toughness of the BMG at different annealing temperature was studied along with the change in isoconfigurational shear modulus and other elastic constants, and the possible origin of the fracture toughness variation is discussed in terms of the ability of the material to overcome the barriers for plastic flow.

4.2 Experimental

The specimen preparation and fracture toughness measurement procedures are described in the previous chapters (Chapters 2 and 3). The $Zr_{44}Ti_{11}Cu_{20}Be_{25}$ alloy, which in the previous chapters is found to have the highest measured as-cast fracture toughness, $K_{Q}=85 \text{ MPa}\cdot\text{m}^{1/2}$, was annealed at various temperatures around and below the calorimetric T_g for durations adequate to achieve structural relaxation: 350°C for 2 hrs, 320°C for 25 hrs and 290°C for 62 hrs. The

calorimetric glass transition temperature (T_g) of the alloy is 340°C [12]. The thermal properties of all specimens were evaluated using differential scanning calorimetry (DSC) at a heating rate of 20K/min. X-ray analysis was performed on a X'Pert Pro x-ray diffractometer to confirm the amorphous nature of annealed specimens. LEO 1550 VP field emission scanning electron microscope was used for fracture surface observation. The pulse-echo overlap technique with 25MHz piezoelectric transducers was used to measure the shear and longitudinal wave speeds at room temperature enabling calculation of the room-temperature elastic constants. Densities were measured by the Archimedean technique according to the ASTM C693-93.

4.3 Fracture toughness of annealed specimens

Figure 4-2 shows fracture toughness data for the annealed specimens together with that for the as-cast specimen. Fracture toughness is shown to decrease linearly with decreasing annealing temperature as the glass relaxes into lower energy configurations. When the alloy is annealed at 290°C, 50°C below T_g , the fracture toughness drops to 6 MPa·m^{1/2}, while retaining its glassy structure. Figure 4-3 shows the X-ray diffraction patterns of all annealed specimens, and reveals that no crystallization is detected in any of the specimens. Figure 4-4 shows the DSC curves acquired from each fracture specimen. Enthalpy recovery around glass transition point is observed for each annealed specimen. The heat of crystallization measured for the as-cast and annealed specimens is 131.6-132.8 J/g (see Table 4-1); this, along with X-ray diffraction verifies that these alloys mostly remain amorphous during annealing.

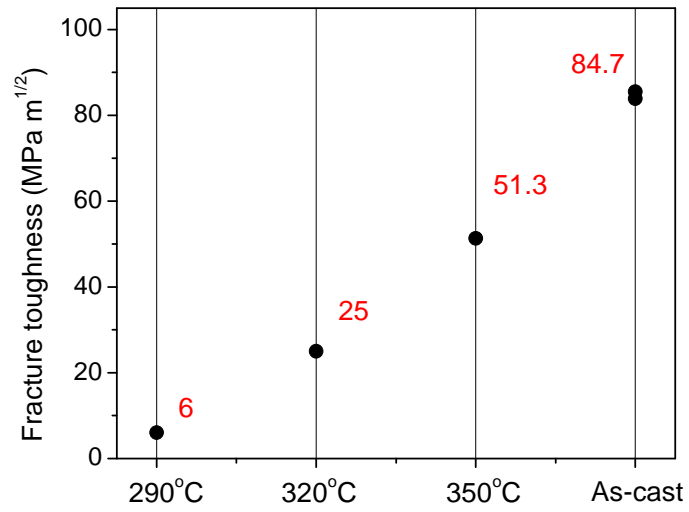


Figure 4-2. Effect of annealing on fracture toughness of Zr₄₄Ti₁₁Cu₂₀Be₂₅ alloy.

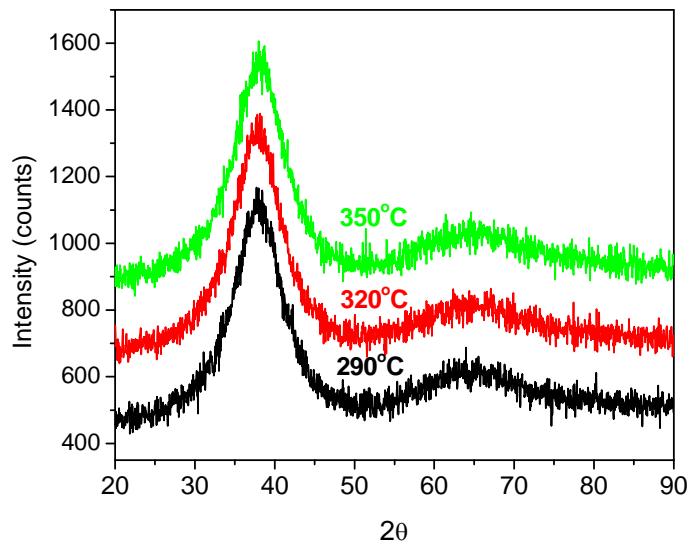


Figure 4-3. X-ray diffraction patterns of specimens annealed at different temperatures.

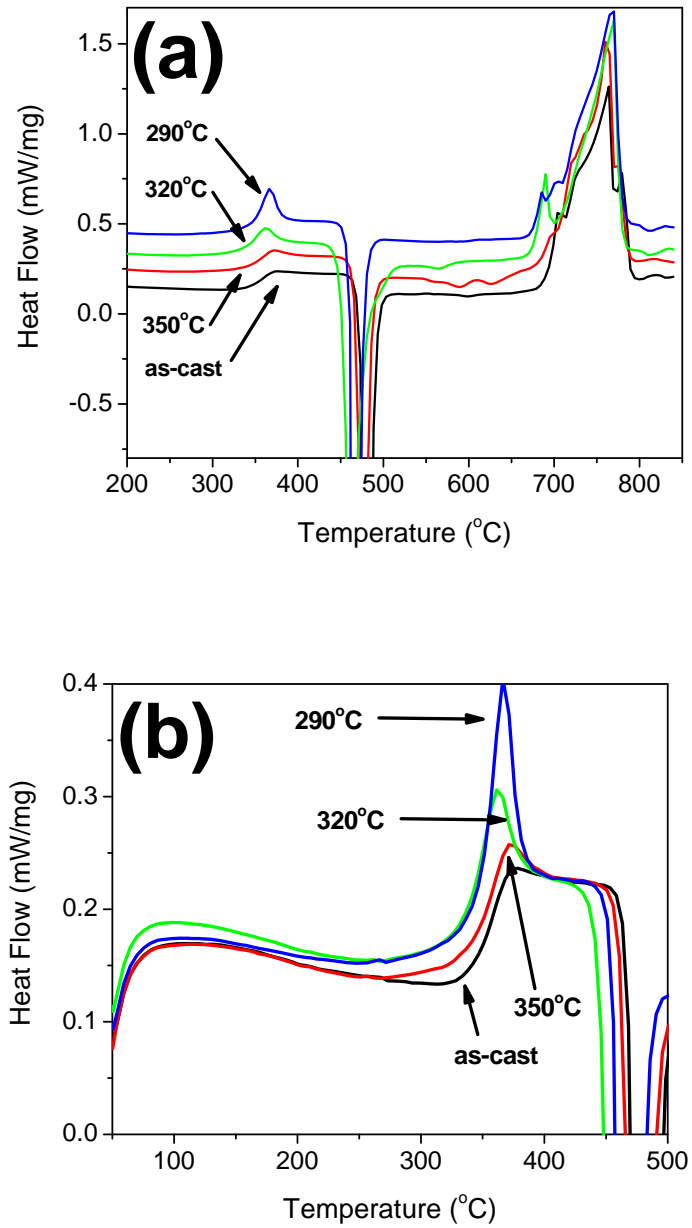
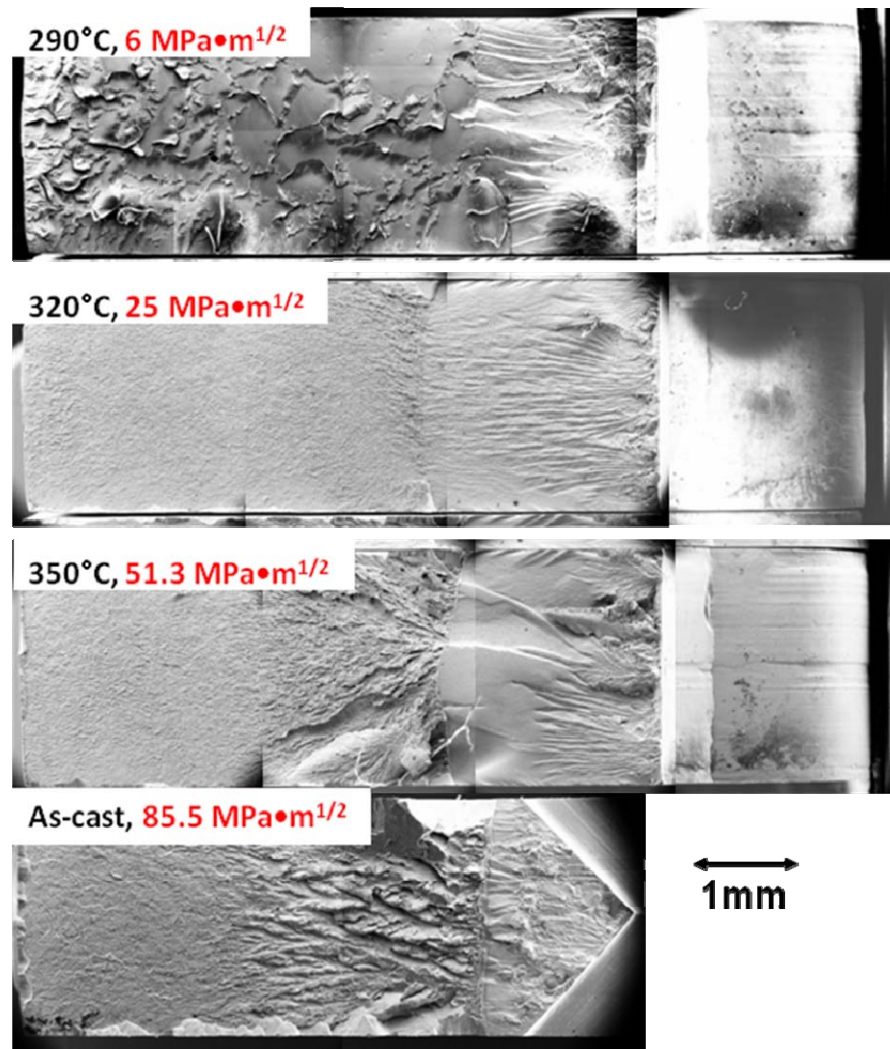


Figure 4-4. DSC curves of as-cast and annealed fracture specimens. (a) overall and (b) magnified images.

Table 4-1. Measured thermal properties of as-cast and annealed specimens.

	T_g (°C)	T_x (°C)	H_{crystal} (J/g)	T_m (°C)	H_{fusion} (J/g)
as-cast	340.8	470	132.3	689.5	173.3
350°C	341.3	468.9	131.6	682.2	177.9
320°C	335.6	450.6	132	675.6	182.3
290°C	347.6	458.5	132.8	674.5	187.9

Figure 4-5. Fracture surfaces of annealed and as-cast $\text{Zr}_{44}\text{Ti}_{11}\text{Cu}_{20}\text{Be}_{25}$ alloy.

The fracture surfaces shown in Figure 4-5 of the annealed specimens are in agreement with the surface features described in Figure 3-2 in chapter 3. The viewpoint of the observation is described in Figure 3-1(b). The fracture surface of the specimen annealed at 350°C, which has fracture toughness of 51.3 MPa·m^{1/2}, has almost the same surface features as shown in Figure 3-2(d). The specimen annealed at 320°C, with $K_Q = 25$ MPa·m^{1/2}, has a uniform fracture surface covered with dimples as shown in Figure 3-2(f) and (g). The fracture surface of the specimen annealed at 290°C is unique. It looks like a cleavage fracture surface having exactly the same features shown by Suh et al [2, 3]. High magnification observation of this surface reveals a uniform dimple structure, with dimples less than 100nm in diameter (see Figure 3-3(d)). These extremely small dimples were also reported by Xi et al [13]. Annealing metallic glass allows the structure to relax into a lower energy configuration, such that it has a higher barrier to flow, and consequently, a reduced resistance to fracture. Considering that the jagged pattern observed in the region adjacent to the notch is primarily the result of shear bands, as discussed in chapter 3, it is conceivable that fracture toughness should be closely related to the ability of the metallic glass to undergo shear and flow.

4.4 Elastic property changes due to annealing of the Zr₄₄Ti₁₁Cu₂₀Be₂₅ alloy

The transient structural relaxation behavior of Zr₄₄Ti₁₁Cu₂₀Be₂₅ alloy is observed by carrying out consecutive steps of annealing of as-cast specimens. A cast rod of Zr₄₄Ti₁₁Cu₂₀Be₂₅ alloy with a diameter of 6 mm is sectioned into disk specimens of height of around 8~9 mm for annealing experiments. The density and elastic properties of each specimen were measured before (as-cast) and after each annealing step. The change in density and elastic properties as a function of annealing time is evaluated by using the same specimen for all annealing steps at each

temperature, in order to maintain consistency with the specimen preparation conditions. The specimens were isothermally annealed under argon in sealed quartz tubes in a tube furnace. For the transient relaxation experiments, two temperatures were considered: 320 and 350°C. These temperatures are also used for the fracture toughness study in the previous section. Two as-cast specimens with a density of 6.027 g/cc were used, having room temperature shear moduli of 35.1 and 35.3 GPa. Because these elastic properties are measured at room temperatures, the effect of thermal expansion has to be considered. The effect of thermal expansion, known as Debye-Grüneisen (DG) effect, is independent of the configurational state. Lind et al. found average DG shear modulus slope $[dG/dT]_{DG} = -0.009115$ GPa/K and average DG bulk modulus slope $[dB/dT]_{DG} = -0.006815$ GPa/K for Vitreloy 4 ($Zr_{46.25}Ti_{8.25}Cu_{7.5}Ni_{10}Be_{27.5}$) [10]. Figure 4-6 shows changes of DG corrected elastic properties as a function of annealing time at both temperatures. As-cast shear moduli of both specimens are corrected to be 32.2 and 32.4 GPa with a reference temperature of 340°C, the calorimetric T_g . For the specimen annealed at 350°C, small changes in elastic properties within a range of experimental errors are detected due to the proximity of the annealing temperature to T_g . Although the T_g of this alloy measured at 20K/min DSC scan is 340°C, the specimen in its as-cast state appears to have a lower shear modulus, and hence higher configurational energy, than in the state equilibrated at 350°C. The enthalpy relaxation of the fracture specimen annealed at 350°C, as shown in Figure 4-4(b), also supports that the specimen equilibrated at 350°C is at lower energy configuration than the as-cast specimen. The transition relaxation at 320°C results in more distinct changes in elastic properties. The shear modulus and bulk modulus increase, but Poisson's ratio decreases. Full equilibration is attained in less than 300 minutes. The transient relaxation of shear modulus at this temperature follows the known stretched exponential function [10].

The equilibrium shear moduli at 320°C (593 K) and 350°C (623 K) are 33.8 and 35.5 GPa, respectively, which yields dG_e/dT is -42 MPa/K. This slope is close to that of Vitreloy 4, which is tabulated in Table 4-2 [9]. Dividing dG_e/dT with the slope of the enthalpy with respect to temperature $d\Delta h/dT$, which can be approximated by the change in heat capacity at T_g , Δc_p , the change in the shear modulus with respect to changes in configurational potential energy can be estimated:

$$(dG/d\Delta h) \cong (dG_e/dT)|_{T_g} / \Delta c_p \quad \text{Equation 4-1.}$$

Although dG/dT of the $Zr_{44}Ti_{11}Cu_{20}Be_{25}$ alloy is close to that of Vitreloy 4, Δc_p , however is smaller, and hence the dependence of isoconfigurational shear modulus on configurational potential energy is as large as that of the Pt-based BMG. According to the cooperative shear model developed by Johnson and Samwer [14], the barrier height for shear flow for a given glass or liquid configuration is proportional to the shear modulus, G . Also, the viscosity of a metallic glass has a unique functional relationship with the shear modulus [9, 11]. This viscosity-shear modulus relationship implies that softening of metallic glass-forming liquids induced by either thermal excitation (by varying temperature) or mechanical deformation (by varying strain rate) is governed by the dependence of isoconfigurational shear modulus on configurational potential energy [9]. Thus, it can be said that the ability of the $Zr_{44}Ti_{11}Cu_{20}Be_{25}$ alloy to soften with increasing configurational energy is comparable to that of Pt-based BMG. Interestingly, the fracture toughness of the Pt-BMG is reported to be $K_Q \cong 80 \text{ MPa}\cdot\text{m}^{1/2}$ [15], that is, comparable to the $Zr_{44}Ti_{11}Cu_{20}Be_{25}$ alloy investigated here, which is found to have a fracture toughness of $K_Q = 84.7 \text{ MPa}\cdot\text{m}^{1/2}$. Since the fracture toughness is thought to be closely related to the ability of the BMG to undergo a certain amount of plasticity prior to failing by catastrophic fracture, as discussed in chapter 3, a correlation between $dG/d\Delta h$ and the fracture toughness is therefore conceivable.

Table 4-2. Relationship between calorimetric and ultrasonic data [9].

Metallic Glass-Forming Liquid	Specific Heat Capacity Change, Δc_p (MJ/m ³ K)	dG_e/dT (MPa/K)	$(dG/d\Delta h) _{th}$
Pt _{57.5} Ni _{5.3} Cu _{14.7} P _{22.5}	2.56	-80	-31.3
Pd ₄₃ Ni ₁₀ Cu ₂₇ P ₂₀	2.5	-60	-24.0
Zr _{46.25} Ti _{8.25} Ni ₁₀ Cu _{7.5} Be _{27.5}	1.7	-35	-20.6
Zr ₄₄ Ti ₁₁ Cu ₂₀ Be ₂₅	1.22	-42	-34.4

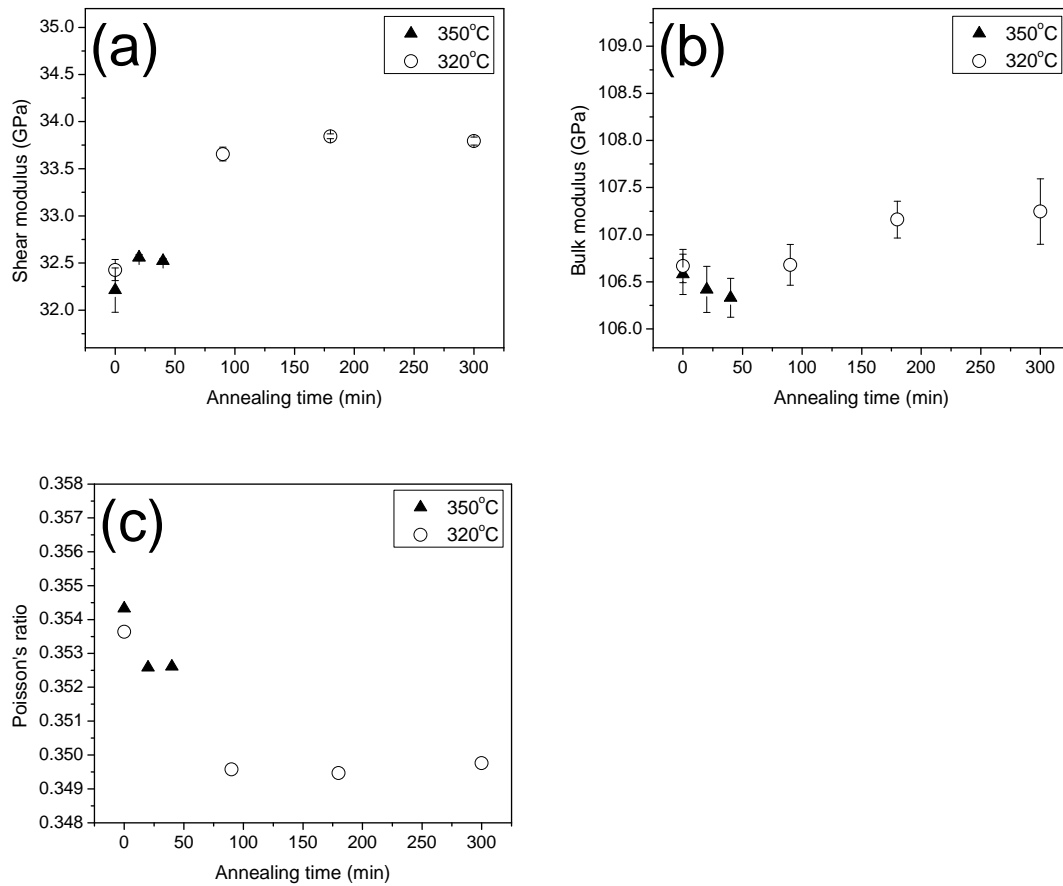


Figure 4-6. Change of elastic constants with annealing at 320 and 350°C.

4.5 Comment on the universal correlation between the energy of fracture and the Poisson's ratio (or the elastic modulus ratio, G/B)

An interesting observation regarding the fracture toughness of the BMG is the dependence of fracture toughness on Poisson's ratio suggested by Lewandowski et al [16]. They proposed a universal correlation between the energy of fracture and the Poisson's ratio (or the elastic modulus ratio G/B) for various metallic glasses. Most importantly, they argued that the fracture toughness data for annealed BMG's fit in the universal correlation perfectly. Their argument attracted a lot of interest because of its conceptual foundation, i.e., fracture process being a competition between plastic flow (determined by shear modulus, G) and fracture opening (determined by bulk modulus, B).

Simple extrapolation of the room temperature elastic properties to the annealed structure at 290°C yields $G = 35.1$, $B = 108.1$ GPa and $\nu = 0.346$. As plotted in Figure 4-7, the Poisson's ratio decreases as the annealing temperature decreases, while the bulk and shear moduli increase. Increase of bulk modulus by lowering the equilibration temperature was also observed by Lind et al [10]. The change of the Poisson's ratio (or G/B) in correlation with the fracture energy agrees with the proposed universal correlation. However, it is noteworthy that, as a liquid structure equilibrates to a lower energy state, G/B increases because shear modulus increases more than bulk modulus does, not because of the increase of shear modulus and decrease of bulk modulus. Thus, the embrittlement of a bulk metallic glass as a function of configurational energy state can be attributed to the dominance of the change of shear modulus, which is a direct measure of the barrier height for shear flow for a given glass or liquid configuration, rather than the competition between plastic flow (determined by shear modulus, G) and fracture opening (determined by bulk modulus, B). This argument also agrees with the observation of chapter 3 that the fracture

toughness of the BMG is closely related to the ability of the BMG to undergo a certain amount of plasticity prior to failing by catastrophic fracture.

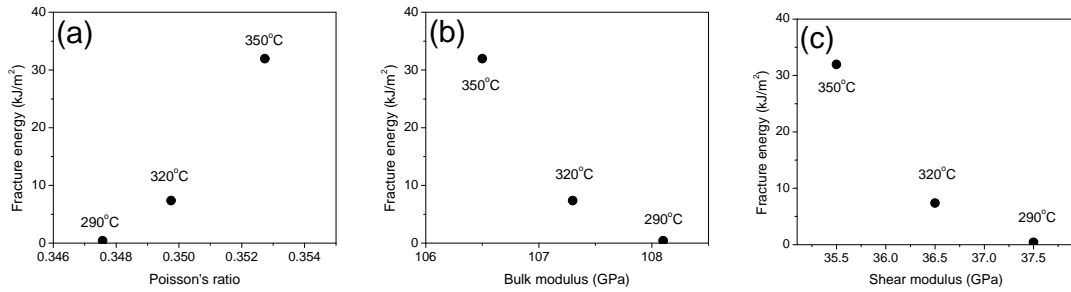


Figure 4-7. Effect of room temperature (a) Poisson's ration, (b) Bulk modulus, and (c) Shear modulus on measured fracture energy (Fracture Energy = $K^2/E/(1-\nu^2)$).

4.6 Conclusions

Fracture toughness decreases as the glass relaxes into lower energy configurations. As a BMG relaxes into lower energy state, shear modulus and bulk modulus increases while Poisson's ratio decreases. Fracture toughness variation in a set of specimens with the same composition can be attributed to the increase of shear modulus based on the cooperative shear model, because the fracture toughness is closely related to the ability of the BMG to undergo a certain amount of plasticity prior to failing by catastrophic fracture.

Acknowledgements

The authors would like to thank Prof. G. Ravichandran of GALCIT, Caltech for providing the MTS test system. This work was supported in part by the MRSEC Program of the National Science Foundation under Award Number DMR-0520565.

References

- [1] C.A. Schuh, T.C. Hufnagel and U. Ramamurty, *Acta Mater.* 55 (2007) 4067.
- [2] D. Suh and R.H. Dauskardt, *Ann. Chim. Sci. Mat.* 27 (2002) 25.
- [3] D. Suh and R.H. Dauskardt, *J. Non-Cryst. Solids* 317 (2003) 181.
- [4] U. Ramamurty, M.L. Lee, J. Basu and Y. Li, *Scripta Mater.* 47 (2002) 107.
- [5] P. Murali and U. Ramamurty, *Acta Mater.* 53 (2005) 1467.
- [6] M.E. Launey, R. Busch and J.J. Kruzic, *Acta Mater.* 56 (2008) 500.
- [7] A. Peker, W.L. Johnson, *Appl. Phys. Lett.* 63 (1993) 2342.
- [8] C.C. Hays, C.P. Kim, W.L. Johnson, *Appl. Phys. Lett.* 75 (1999) 1089.
- [9] W.L. Johnson, M.D. Demetriou, J.S. Harmon, M.L. Lind and K. Samwer, *MRS Bull.* 32 (2007) 644.
- [10] M.L. Lind, G. Duan and W.L. Johnson, *Phys. Rev. Lett.* 97 (2006) 015501.
- [11] M.D. Demetriou, J.S. Harmon, M. Tao, G. Duan, K. Samwer and W.L. Johnson, *Phys. Rev. Lett.* 97 (2006) 065502.
- [12] C.P. Kim, J.-Y. Suh, A. Wiest, M.L. Lind, R.D. Conner and W.L. Johnson, *Scripta Mater.* 60 (2008) 80.
- [13] X.K. Xi, D.Q. Zhao, M.X. Pan, W.H. Wang, Y. Wu and J.J. Lewandowski, *Phy. Rev. Lett.* 94 (2005) 125510.

- [14] W.L. Johnson and K. Samwer, Phys. Rev. Lett. 95 (2005) 195501.
- [15] J. Schroers and W.L. Johnson, Phys. Rev. Lett. 93 (2004) 255506.
- [16] J.J. Lewandowski, W.H. Wang and A.L. Greer, Phil. Mag. Lett. 85 (2005) 77.